Food Hydrocolloids 126 (2022) 107442

Contents lists available at ScienceDirect

Food Hydrocolloids

journal homepage: www.elsevier.com/locate/foodhyd

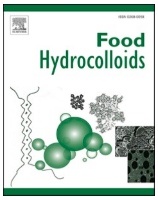

Rheological behaviour of concentrated maltodextrins describes skin formation and morphology development during droplet drying

I. Siemons [a], J. Veser [a], R.M. Boom [a], M.A.I. Schutyser [a], R.G.M. van der Sman [a,b,*]

[a] Laboratory of Food Process Engineering, Wageningen University and Research, P.O. Box 17 6700, AA, Wageningen, the Netherlands
[b] Food Biobased Research, Wageningen University and Research, P.O. Box 17 6700, AA, Wageningen, the Netherlands

ARTICLE INFO

Keywords:
Rheology
Polysaccharides
Master curve
Single droplet drying
Morphology development

ABSTRACT

We have studied the rheological behaviour of concentrated maltodextrins varying in dextrose equivalence value (DE) over a range of temperatures (≤70 °C) and concentrations (≥62% (w/w) solids) using small amplitude oscillatory experiments. Rheological data could be mapped onto master curves for storage and loss modulus as described with a model for transient or entangled polymeric networks. Maltodextrins DE5 and DE12 showed a rubber-to-glass transition, where the rubber-like behaviour is hypothesized to be the consequence of physical entanglements at sufficiently high concentrations of polysaccharides. Maltodextrins DE21 and DE38 mostly consisting of small sugars and oligomers exhibited viscous behaviour over a large range of frequencies and only at high frequencies the onset of a cross-over was visible which could signify the vicinity of the glass transition. An effective diffusion drying model validated with sessile single droplet drying experiments was coupled to rheological models to estimate rheological behaviour during droplet drying. The predicted rheological properties of the skin formed at the surface of the droplet could be related to the occurrence of surface instabilities later during drying, including cavitation for elastic skins and wrinkling for viscous skins. Insight in rheological behaviour at high concentrations may therefore offer help in predicting the morphology of droplets generated with spray drying.

1. Introduction

The rheological behaviour of concentrated food systems is of importance for the design and optimisation of both processes and product properties. Examples of operations that involve materials that are concentrated in carbohydrates and/or proteins are extrusion, coating, evaporation and spray drying. In spray drying, the rheological behaviour of the concentrated feed solution is critical for the atomization into fine droplets, but also influences the particle structure evolution and agglomeration behaviour during drying, concomitantly co-determining the final powder properties (Both, Tersteeg, Boom, & Schutyser, 2019 b; Finotello et al., 2017; Porfirio, Galindo-Rosales, Campo-Deaño, Vicente, & Semião, 2020; Ubbink & Dupas-Langlet, 2020).

Various investigations studied the rheological behaviour of concentrated systems to provide better mechanistic insight of skin formation and subsequent morphology development during spray drying (Both et al., 2019 b; Le Floch-Fouéré et al., 2019; Sadek et al., 2015; Sugiyama, Larsen, Kim, & Weitz, 2006). For this, studies employed single droplet drying under controlled conditions to mimic the spray drying environment. For skin forming materials, the emergence of the rheological properties of the skin that is forming at the surface of the droplet during drying is hypothesized to be critical to the formation of wrinkles and/or cavities, and accordingly to the final particle morphology (Du, Ye, Doi, & Meng, 2020; Wang & Cai, 2015). For example, cavity formation during drying of droplets consisting of colloidal dispersions or polymer solutions is suggested to be the result of the formation of an elastic skin that still allows for moisture evaporation (Bouman, Venema, de Vries, van der Linden, & Schutyser, 2016). The continued moisture evaporation through the skin and the resulting reduction of volume of the droplet, causes the skin to be compressed, followed by an increase in the elastic energy of deformation and a resulting lower pressure inside the droplet. The elastic compression is then reduced by the formation of a cavity to comply with the pressure reduction, rather than further shrinkage (Meng, Doi, & Ouyang, 2014). Wrinkling phenomena may occur when droplet skins are thin and do not develop significant elasticity, allowing deformation due to surface compression (Du et al., 2020; Siemons, Politiek, Boom, Sman, & Schutyser, 2020). Wrinkling may in fact be followed by cavitation depending on elastic properties of the skin and the skin thickness developed during drying (Du et al., 2020).

---

* Corresponding author. Food Biobased Research, Wageningen University and Research, P.O. Box 17 6700, AA, Wageningen, the Netherlands.
E-mail addresses: isabel.siemons@wur.nl (I. Siemons), ruud.vandersman@wur.nl (R.G.M. van der Sman).

https://doi.org/10.1016/j.foodhyd.2021.107442
Received 14 April 2021; Received in revised form 17 November 2021; Accepted 9 December 2021
Available online 15 December 2021

In our previous study, we employed small amplitude oscillatory shear (SAOS) on concentrated thin maltodextrin films, which provided valuable rheological data that could be related to morphology development of maltodextrins during single droplet drying (Both, Siemons, Boom, & Schutyser, 2019 a; Siemons et al., 2020). However, rheology experiments were only performed for films at one concentration and with a fixed temperature. As moisture content and temperature are continuously evolving during drying, it is important to assess the rheological behaviour over a wider range of concentrations and temperatures.

The rheology that needs to be investigated for drying spans a large range of conditions, to allow this, superposition principles may be used to connect the influences of time (frequency), temperature and concentration. To do this, one can study the frequency-dependent properties of materials, including storage (G′) and loss (G″) modulus. The time-temperature superposition principle (TTSP) then poses, that the effects of time and temperature are related and can be combined in a master curve showing rheological behaviour covering a broad range of frequencies (Dealy & Plazek, 2009). For constructing a master curve, rheological data for one temperature and frequency are translated to the equivalent response at a different temperature by multiplying the frequency with a temperature-dependent shift factor (Dealy & Plazek, 2009; Kasapis, 2001). Several researchers already showed for various concentrated carbohydrate systems that master curves using TTSP can be constructed (De Freitas et al., 2015; Kasapis, 2001; Palzer, 2010; Tsoga, Kasapis, & Richardson, 1999). In more recent work by Van der Sman, Dupas-Langlet, Ubbink, Kristiawan, and Siemons (2021), it was demonstrated for concentrated polysaccharides that the superposition principle could be extended to different frequencies, temperatures and concentrations, using the glass transition temperature divided by the temperature (T_g/T) as scaling parameter. The master curves constructed in the latter work partially resembled the universal master curve for entangled polymers (Groot & Agterof, 1995; Sperling, 2001), showing three zones: a rubbery plateau zone, a transition zone from rubber-like to glass-like behaviour and a glassy zone.

Here, we study the effects of time (frequency), temperature and concentration on the rheological behaviour of concentrated maltodextrins varying in dextrose equivalence value using SAOS testing. We constructed master curves, which map the rheological behaviour of maltodextrins at various temperatures and concentrations in a single plot. Master curves were described with a model for transient or entangled networks (Marin & Graessley, 1977). Horizontal shift factors, incorporating both the effect of temperature and concentration were collected. Finally, to discuss the added value of the obtained rheological insights, we discuss how the rheological behaviour can be connected to morphology development during drying. The latter was done on the basis of modelling of the temperature and moisture evolution during droplet drying, using an effective diffusion drying model validated with sessile single droplet drying experiments.

2. Materials and methods

2.1. Materials

Maltodextrins with dextrose equivalence (DE) 5, 12, 21 and 38 were purchased from Roquette Frères (Lestrem, France). Solutions were prepared at a dry matter concentration of 30% (w/w) by adding maltodextrin powder to demineralized water and stirring for at least 30 min until the solution was transparent.

2.2. Preparation of concentrated samples and thin films

Concentrated maltodextrin samples were prepared by rotary evaporation or thin film preparation (Both et al., 2019 b; Both, Tersteeg, Schutyser, & Boom, 2019 c; Siemons et al., 2020). Rotary evaporation was performed to reach intermediate concentrations (~60–85% (w/w) solids depending on DE), while thin films were prepared to reach higher concentrations close to the glassy state (~80–95% (w/w) solids depending on DE).

The rotational evaporator (RC900, KNF, Germany) was operated at 30–70 mBar at 50–70 °C to concentrate 30% (w/w) maltodextrin solutions. Concentrated solutions were deaerated for 10 min to remove the entrapped air in an ultrasonic bath (5210E-DTH, Branson, USA). Thin maltodextrin films were prepared with an initial dry matter of 30–60% (w/w), followed by an equilibration step in a climate chamber (Memmert, Germany) at 50 °C for 3 day as was described by Siemons et al. (2020). Samples were directly tested after sample preparation to prevent nucleation of crystallites. If the samples turned turbid, they were not used for rheological experiments. The thin films varied in dry matter concentration depending on the set relative humidity of the climate chamber (Table A.1).

2.3. Small amplitude oscillatory shear testing

Small amplitude oscillatory shear (SAOS) was used to determine the linear viscoelastic properties of concentrated maltodextrin systems using a MCR 502 Rheometer (Anton Paar, Austria). Thin film rheology measurements were performed using a parallel plate geometry with a ribbed probe with a diameter of 25 mm, 1N force control. Maltodextrins concentrated with rotary evaporation were tested with stainless steel cone plate geometry with a diameter of 50 mm. A thin layer of paraffin oil was applied on the edge of the sample in order to prevent moisture loss during the measurements. Samples were allowed to rest and equilibrate for 15 min before testing. Amplitude sweeps were performed to determine the extent of the LVE region with a shear strain range of 0.01–100.00% with constant angular frequency set at 1 rad/s for thin films and 10 rad/s for rotary evaporation samples. For frequency sweep tests a frequency range of 0.1–100 rad/s was used at fixed strains within the LVE region. Tests were carried out with a temperature range below 80 °C. An overview of all SAOS data is given in the supplementary data (Figs. S1–S6).

2.4. Constructing master curves

Master curves for G′ and G″ were constructed in an iterative manner using a customized Python algorithm (Van der Sman et al., 2021). The algorithm aims to match SAOS data at different temperatures and concentrations to the Marin-Graessley (MG) model for transient/entangled networks (Marin & Graessley, 1977). In this model the complex compliance ($J^* = 1/G^*$ and $G^* = G' + iG''$ with $i = \sqrt{-1}$) is given by:

$$J^*(\omega) = J_\infty\left[1 + \frac{1}{i\omega\tau_M} + \frac{k_p}{1+(i\omega\tau_p)^p} + \frac{k_\alpha}{1+(i\omega\tau_\alpha)^\alpha}\right] \tag{1}$$

where J_∞ (Pa^{-1}) is the compliance in the glassy regime ($J_\infty = \frac{1}{G_\infty}$), the first two terms of equation (1) represent Maxwell (viscoelastic) relaxation, the third term modifies the response in the plateau zone and the last term represents the α-relaxation (segmental relaxation). The latter two terms are expressions following a Cole-Cole type relaxation model. τ_M (s) is the relaxation time of the Maxwell relaxation mode, τ_p (s) is a characteristic relaxation time and τ_α (s) is the relaxation time of the α-relaxation. k_p and k_α (−) are related to the amplitudes in the plateau and transition zones, respectively. The scaling exponent α determines the shape of the curve in the transition zone, exponent p influences the shape of the curve in the plateau zone.

For matching SAOS data to the MG model, a method of least squares was used:

$$\begin{aligned} L_2 = \sum_i w_1\left[\log\left(G'_{ref,i}(w_{ref})\right) - \log\left(G'_{new,i}(\omega w a_T)\right)\right]^2 \\ + w_2\left[\log\left(G''_{ref,i}(w_{ref})\right) - \log\left(G''_{new,i}(\omega w a_T)\right)\right]^2 \end{aligned} \tag{2}$$

$G_{ref,i}$ represents the reference master curve of the MG model, and $G_{new,i}$ represents the experimental data with frequencies shifted by horizontal shift factor a_T ($\omega w a_T = w_{ref}$). w_1 and w_2 are weight factors, which we have chosen as $w_1/w_2 \approx 2$.

Horizontal shift factors a_T used to minimize the distance between the reference master curve of the MG model and experimental data were stored as a function of temperature divided by glass transition temperature (T_g/T). T_g was estimated as function of moisture content using the Couchmann-Karasz model (Couchman & Karasz, 1978) as was previously also reported in (Siemons et al., 2020):

$$T_g = \frac{y_w \Delta c_{p,w} T_{g,w} + y_s \Delta c_{p,s} T_{g,s}}{y_w \Delta c_{p,w} + y_s \Delta c_{p,s}} \tag{3}$$

Here y_i is the mass fraction ($i = w, s$ for water and solute), $T_{g,i}$ is the glass transition temperature for the pure component ($T_{g,w} = 139$ K), $\Delta c_{p,i}$ is the change in the specific heat at the glass transition ($\Delta c_{p,w} = 1.91$ kJ/kg·K, $\Delta c_{p,s} = 0.42$ kJ/kg·K) (Van Der Sman & Meinders, 2011, 2013).

The glass transition of the anhydrous maltodextrin, $T_{g,s}$, can be described by the Flory-Fox relation (Avaltroni, Bouquerand, & Normand, 2004; Fox & Flory, 1950; Roos & Karel, 1991; Sman & Meinders, 2012):

$$T_{g,s} = T_{g,s}^{\infty} - \frac{a_{FF}}{M} \tag{4}$$

$T_{g,s}^{\infty}$ (K) is the glass transition temperature for polymers with an infinite polymer chain length ($T_{g,s}^{\infty} = 475$ K), $a_{FF} = 5 \times 10^4$ K·g/mol and $M = 100^* \left(\frac{180}{DE}\right)$ is the number average molecular weight.

2.5. Modelling single droplet drying

The single droplet drying model was based on heat and mass transfer theories similar to previous studies (Adhikari, Howes, & Bhandari, 2007; Mezhericher, Levy, & Borde, 2010; Perdana, Fox, Schutyser, & Boom, 2013; van der Sman, 2003). The droplet has a uniform temperature throughout drying (Biot number (Bi) < 0.4) (Patel & Chen, 2008). Bi represents the ratio of external and internal heat flux, with the external heat transfer coefficient h_{ext} (W·m^{-2}·K^{-1}), the droplet radius r (m) and the effective heat conductivity λ_{eff} (W·m^{-1}·K^{-1}). In this study, Bi is around 0.12.

$$Bi = \frac{h_{ext} r}{\lambda_{eff}} \tag{5}$$

The numerical model is based on the following differential equations for mass and energy transport:

$$\partial_t c_w + \nabla \cdot c_w \overrightarrow{u_s} = \nabla \cdot D_m \nabla c_w \tag{6}$$

$$\partial_t \rho_{eff} c_{p,eff} T + \nabla \cdot \rho_{eff} c_{p,eff} T \overrightarrow{u_s} = \nabla \cdot \lambda_{eff} \nabla T \tag{7}$$

c_i is the mass concentration (kg·m^{-3}), u_i is the velocity of the moving mass (m·s^{-1}) ($i = w, s$ for water and solute), D_m is the mutual moisture diffusion (m^2·s^{-1}), ρ_{eff} is the effective density (kg·m^{-3}), $c_{p,eff}$ is the effective heat capacity (J·kg^{-1} K^{-1}), T is the droplet temperature (K). Note that the above equations hold in the Eulerian frame. We will solve the equations in the co-moving Lagrangian frame of the shrinking droplet. Using the definition of the convective derivative $D_t = \partial_t + \nabla \cdot \overrightarrow{u_s}$, where D_t is the time derivative in the Lagrangian reference frame, the equations can be rewritten in a familiar form of Fick's and Fourier's law:

$$D_t c_w = \nabla \cdot D_m \nabla c_w \tag{8}$$

$$D_t \rho_{eff} c_{p,eff} T = \nabla \cdot \lambda_{eff} \nabla T \tag{9}$$

We will solve the energy and mass balance in spherical coordinates with the cell-centered Finite Volume scheme, using central differencing, and simple Euler forward time integration. As said, the model is solved in the Lagrangian frame of the solid material, meaning that the amount of solids remains constant throughout the computation. Only water will be exchanged between control volumes, which will change the volume of spherical shells. At each time step new positions, volumes and surface areas of the control volumes are computed, which are used to compute the diffusive mass and energy fluxes. For the temperature of the droplet we integrate the energy balance over the whole volume of the droplet.

The initial and boundary conditions are as follows:

$$c_w(r, t=0) = c_{w,0} \quad T(r, t=0) = T_0$$

$$\partial_r c_w(r=0) = 0 \partial_r T(r=0) = 0$$

$$-D_m \partial_r c_w(r=R) = J_{evap} \tag{10}$$

$$-\lambda_{eff} \partial_r T(r=R) = h_{ext}(T - T_{air}) - \left[\ \Delta H_{evap,0} + \left(c_{p,v} - c_{p,w}\right)(T - T_0)\ \right] J_{evap} \tag{11}$$

ρ_{eff}, λ_{eff}, D_m are moisture dependent material properties, with relations shown in Table 1. r is the radial coordinate (m), R is the droplet radius (m), $c_{w,0}$ is the initial water concentration (kg·m^{-3}), T_0 is the reference temperature for the enthalpy for evaporation, being 0 °C, T_{air} is the temperature of the bulk air (K), $\Delta H_{evap,0}$ heat of vaporization of water at 0 °C (J·kg^{-1}), $c_{p,v}$ and $c_{p,w}$ (J·kg^{-1} K^{-1}) the specific heat of vapour and water, respectively.

The evaporative mass flux J_{evap} (kg·s^{-1}) equals:

$$J_{evap} = f_{cap} 4\pi R^2 \beta_{ext} M_w \frac{p_0}{R_{gas} T_{avg}} \ln\left(\frac{p_0 - p_{air}}{p_0 - a_w p_{sat}(T)}\right) \tag{12}$$

f_{cap} is a factor correcting for the fact that the droplet is not spherical, but it is sessile. β_{ext} (m·s^{-1}) is the external mass transfer coefficient, M_w (kg·mol^{-1}) molecular weight of water, p_0 atmospheric pressure, p_{air} air pressure and p_{sat} (Pa) saturation pressure at drop temperature T (K), $T_{avg} = (T_{air} + 2T)/3$ (K) is the estimated average temperature of the boundary layer, a_w is the water activity (–). As we use the cell-centered Finite Volume method we have to estimate c_w and T at the outer surface of the droplet via solving the boundary conditions with an implicit solver (bisection method).

To correct for the supporting plate and consequently the reduced surface area of the sessile single drop (Fig. 1), A_{drop} was calculated based on changing wall angles $\delta = \pi - \theta$ (rad), height of the cap $h_{cap} = r(1 - cos(\delta))$ (m) and height of the drop $H_{drop} = r(1 + cos(\delta))$ (m) (Soh, Yeoh, & Timchenko, 2016):

$$A_{drop} = 4\pi R^2 - 2\pi R h_{cap} = 2\pi R H_{drop} \tag{13}$$

$$f_{cap} = \frac{A_{drop}}{4\pi R^2} \tag{14}$$

Non-uniform air flow and heat transfer were considered as the air flow pattern near the droplet is influenced by the supporting flat plate, although it is thin (Mosaad, 1999; Perdana et al., 2013). For the thickness of the hydrodynamic boundary layer δ_U (m) the distance $x_p = 2.25$ cm from start of the plate until where the droplet was located, the bulk air velocity $U_{air} = 0.3$ m·s^{-1} and the calculated kinematic viscosity of air $\upsilon_{air} = 2.2 \cdot 10^{-5}$ m^2·s^{-1} were used. The air velocity U and the air temperature T near the droplet were calculated using the height $z = R$.

Table 1
Closure equations used in drying model. The values of the parameters are indicated in Table A.2 and for material specific parameters the values can be found in Table S2.

Equation name	Equation	Reference
Diffusion coefficient of water (Free volume theory)	$D_w = D_0 \cdot exp\left(\frac{-dE}{R_{gas}T}\right) \cdot exp\left(\frac{y_w \cdot V_{c,w} + \xi_b \cdot (1-y_w) \cdot V_{c,s}}{B}\right)$ with $B = y_w \cdot K_{w,w} \cdot (K_{s,w} - T_{g,w} + T) + (1 - y_w) \cdot K_{w,s}(K_{s,s} - T_{g,s} + T)$	Vrentas & Vrentas (1991); Siemons et al. (2020); Van Der Sman and Meinders (2013)
Diffusion coefficient of solute (Generalized Stokes Einstein relation)	$D_{s,0} = \frac{k_B \cdot T}{6\pi \cdot \eta_w \cdot a_0}$ with a_0 as the hydrodynamic radius (m)	Miller (1924); Sutherland (1905); Van Der Sman and Meinders (2013)
Effective diffusion coefficient	$D_{eff} = D_{s,0} \cdot \frac{\eta_w}{\eta_{eff}}$ with $\log\left(\frac{\eta_{eff}}{\eta_0}\right) = 4q + 11q^2 + 10q^3$ and $q = \frac{T_g}{T - 0.35}$	van der Sman & Mauer (2019)
Mutual diffusion coefficient Darken relation	$D_m = Q_D \cdot (\varphi_w D_{eff} + (1 - \varphi_w) \cdot D_w)$ with $\varphi_w = \frac{V_w}{V_{tot}}$ volume fraction of water (−) with $V_{tot} = 1/\rho_{eff}$	Darken (1948); Siemons et al. (2021); Perdana et al. (2013)
Water activity Flory-Huggins theory	$a_w = \exp\left(\frac{\mu_w}{R_{gas}\ T}\right) = \exp\left(\ln(\varphi_w) + \left(1 - \frac{1}{N_s}\right) \cdot (1 - \varphi_w) + \chi_{eff} \cdot (1 - \varphi_w)^2\right)$ $\chi_{eff} = \begin{cases} \chi_{ws} & ,\chi_{ws} \leq \chi_0 \\ \chi_{ws} - (\chi_{ws} - \chi_0) \cdot (\varphi_w)^2 & ,\chi_{ws} > \chi_0 \end{cases}$ with N_s the ratio of molar volume of solvent and solute, χ_{eff} the effective interaction parameter (−), χ_{ws} the interaction parameter of maltodextrin	Fox and Flory (1950); (1953); Van Der Sman and Meinders (2011)
External mass transfer coefficient	$\beta_{ext} = f_\alpha \frac{ShD_{air}}{2R}$	
Sherwood number (Ranz Marshall)	$Sh = 2 + 0.6Re0.5Sc^{0.33} = 2 + 0.6\left(\frac{U2R}{\nu_{air}}\right)^{0.5}\left(\frac{\nu_{air}}{D_{air}}\right)^{0.33}$	Ranz & Marshall (1952); (2007)
Alpha correction factor (Film theory)	$f_\alpha = \frac{\ln\left(1 + \frac{a_w p_{sat}(T) - p_{air}}{p_0 - p_{air}}\right)}{\frac{a_w p_{sat}(T) - p_{air}}{p_0 - p_{air}}}$	Bird et al. (1960); Adhikari et al. (2007)
Heat transfer coefficients	$h_{eff} = \frac{1}{\frac{1}{h_{int}} + \frac{1}{h_{ext}}}$ with $h_{ext} = \frac{Nu\lambda_{air}}{2R}$ and $h_{int} = \frac{\lambda_{eff}}{0.5r}$	
Thermal conductivity	$\lambda_{eff} = \varphi_w \lambda_w + \varphi_s \lambda_s$	
Effective density	$\rho_{eff} = \frac{1}{vspec} = \frac{1}{\frac{y_w}{\rho_w} + \frac{1 - yw}{\rho_s}}$	
Nusselt number Ranz Marshall	$Nu = 2 + 0.6Re0.5Pr^{0.33} = 2 + 0.6\left(\frac{U2R}{\nu_{air}}\right)^{0.5}\left(\frac{\nu_{air}}{\alpha_{air}}\right)^{0.33}$ with α_{air} as thermal diffusivity of air ($m^2 \cdot s^{-1}$)	Adhikari et al. (2007)

Table 2
Fitted model parameters for maltodextrins varying in dextrose equivalence (DE). DE2 data was obtained from Van der Sman et al. (2021) for comparison. Note that *a* and *b* are defined by the reference temperature for the shift factor, reference temperatures differ for the different DEs.

Marin-Graessley parameters	DE5	DE12	DE21	DE38	DE2
τ_M (s)	10^3	10^2	10^3	10^3	10^3
τ_α (s)	0.5	0.5	$1 \cdot 10^{10}$	$1 \cdot 10^{12}$	0.5
τ_p (s)	$2 \cdot 10^3$	$6 \cdot 10^3$	–	–	–
k_α (−)	$3.5 \cdot 10^3$	$11 \cdot 10^3$	$8 \cdot 10^{16}$	$2 \cdot 10^{17}$	$3 \cdot 10^{-3}$
k_p (−)	$7 \cdot 10^2$	10^3	–	–	–
G_∞ (Pa)	$6 \cdot 10^8$	$1.5 \cdot 10^8$	$4 \cdot 10^7$	$4 \cdot 10^8$	$1 \cdot 10^9$
α (−)	0.65	0.60	0.93	0.85	0.60
p (−)	0.25	0.35	–	–	–
Linear fit shift factors					
a (−)	2.42	2.43	2.89 –	1.61	
b (−)	– 6.64	– 6.63	5.30	– 3.76	

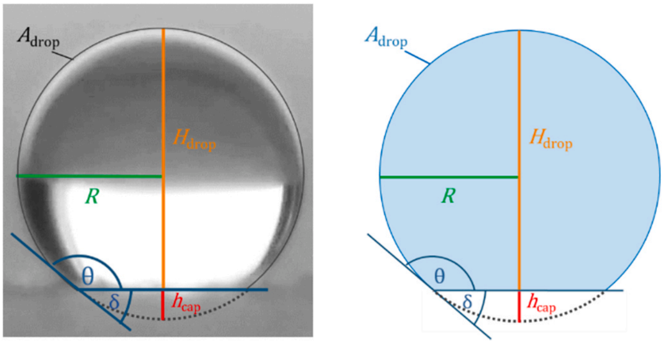

Fig. 1. Geometry of sessile single drop as a sphere without cap with drop surface area A_{drop}, drop height H_{drop}, drop radius R, cap height h_{cap} as well as wall angle of droplet θ and of cap δ.

$$\delta_U = 5\sqrt{\frac{\upsilon_{air} x_p}{U_{air}}} \tag{15}$$

$$\frac{U}{U_{air}} = \frac{3}{2}\left(\frac{z}{\delta_U}\right) - \frac{1}{2}\left(\frac{z}{\delta_U}\right)^3 ; 0 \leq z \leq \delta_U \tag{16}$$

For the thickness of the thermal boundary layer δ_t, the Prandtl *Pr* number is necessary. The temperature of the plate at distance x_p ($T_{p,x}$) was 70 °C (Table S1).

$$\delta_t = \begin{cases} Pr^{-\frac{1}{3}}, & Pr \leq 1 \\ Pr, & Pr > 1 \end{cases} \tag{17}$$

$$\frac{T - T_{air}}{T_{p,x} - T_{air}} = 1 - \frac{3}{2}\left(\frac{z}{\delta_t}\right) + \frac{1}{2}\left(\frac{z}{\delta_t}\right)^3 ; 0 \leq z \leq \delta_t \tag{18}$$

The model was implemented in Python 3.8.3 with the programme Spyder 4.1.5 (Anaconda Inc., USA). Model parameters and material parameters are provided (Table A.2, Tables S1 and S2). The model was validated with single droplet drying experiments as described by Siemons et al. (2020, 2021). The experimental radius decrease and wall angles were obtained via image analysis toolbox from Matlab (Mathworks, USA) as described by Both, Karlina, Boom, and Schutyser (2018). Videos were analysed from the onset of drying until the mean locking point times for each DE as reported in previous work (Siemons et al., 2020). The locking point is the first visual deviation from the original spherical droplet shape and represents an indirect indication for the inception of the skin. From this point onwards the morphology starts to develop. Fits were obtained for three videos for the DE-values (Figs. S7 and S8). The model assumes uniform evaporation, i.e. no different local evaporative flux at for instance the contact line, and no circulation flows (e.g. Marangoni) due to high initial viscosities.

2.6. *Connecting rheological model and single droplet drying model*

The connection of drying and rheological data was based on shear rates $\dot{\gamma}$ (s^{-1}) obtained from modelled radius decrease over time $dr/\ dt$ ($m \cdot s^{-1}$). Therefore, the derivative of the modelled drop radius was obtained using the finite difference method with time step $dt = 0.001$ s (Fig. 2).

$$\dot{\gamma} = \frac{dr}{dt} \cdot \frac{1}{r} \tag{19}$$

According to the Cox-Merz rule, a shear rate can be directly translated into angular frequency ω ($rad \cdot s^{-1}$) in the linear viscoelastic range for certain materials, mostly linear homopolymers such as maltodextrins (Augusto, Falguera, Cristianini, & Ibarz, 2013; Cox & Merz, 1958; Dupas-Langlet, Meunier, Pouzot, & Ubbink, 2019; Ishii & Nakamura, 2020; Sillick & Gregson, 2009; Winter, 2009). Therefore, the calculated shear rate was directly translated to an equivalent angular frequency.

Besides shear rates, droplet temperature, glass transition temperature and accordingly horizontal shift factors (a_T) were calculated for each shell and drying time. The latter required fitting of log a_T values obtained from construction of master curves with a linear function of glass transition temperature and drop temperature $\left(\frac{T}{T_g} - 0.77\right)^{-1}$ with fitting parameter a and b (Liu, He, Keunings, & August, 2006).

$$\log a_T = a\left(\frac{T}{T_g} - 0.77\right)^{-1} + b \tag{20}$$

Note, that a and b are not independent parameters, as their relation is defined by the reference temperature for the shift factor. The calculated angular frequencies were multiplied with the calculated horizontal shift factors ($\omega \cdot a_T$) and with this G′ and G″ could be obtained directly with the MG model. The overall calculation procedure for connecting the drying model to the rheological model is depicted in Fig. A.1.

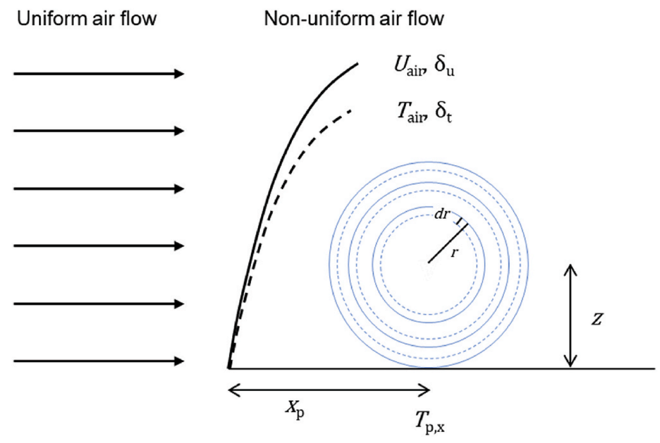

Fig. 2. Schematic illustration of air flow distribution over flat plate with hydrodynamic boundary layer thickness δ_u with bulk air velocity U_{air} and thermal boundary layer thickness δ_t with bulk air temperature T_{air} as well as distance x_p, height z and temperature of plate T_{xp}. The droplet is schematically illustrated with exemplary three different shells with radius decrease dr and outer radius r of each shell. The shells are calculated as spheres, the surface area and the radius of the whole droplet however are calculated as a reduced area and as the radius of a sphere without a cap, accounting for the sessile droplet. This is not shown in this figure.

3. Results and discussion

3.1. *Dependence of viscoelastic behaviour of thin films on temperature*

Small amplitude oscillatory shear data were first collected for maltodextrin thin films at a particular concentration as function of the temperature. The frequency dependence of the storage (G′) and loss (G″) moduli at different temperatures between 20 and 70 °C of maltodextrin thin films varying in dextrose equivalence (DE) are shown in Fig. 3. The moduli of DE5 and DE12 films span roughly three orders of magnitude (Fig. 3A, C); at low temperatures elastic behaviour was observed, while at intermediate temperatures the films showed a transition from viscous behaviour at low frequencies to elastic behaviour at high frequencies. For the highest temperatures, a cross-over from elastic behaviour at low frequencies to viscous behaviour at higher frequencies was observed. DE21 and DE38 thin films showed viscous behaviour over the frequency and temperature range tested (Fig. 3E, G). Only at low temperatures did DE21 films exhibit a transition from viscous to elastic behaviour.

Master curves for G′ and G″ were obtained by shifting the mechanical spectra horizontally along the frequency axis using the superposition algorithm (Fig. 3B, D, F, H). The master curve then describes the viscoelastic properties of the maltodextrin thin films over a broad frequency range. Especially, the sigmoidal transition found for DE5 (Fig. 3B) agrees well with a part of the universal master curve for entangled polymers (Groot & Agterof, 1995); indicating that the films are in a transition zone between rubber-like and glass-like behaviour. At low frequencies the storage modulus is the predominant response, followed by a sharp increase in moduli upon cooling the film. At high frequencies elastic behaviour is again dominant. Similar transition behaviour could be identified for DE12 (Fig. 3D) (G’~G″), although the sigmoidal shape is not as pronounced as for DE5. The rubber-like behaviour is likely the consequence of physical entanglements at sufficiently high concentration of long polymeric chains (Table A.3). According to Levine and Slade (1986) above a critical polymer concentration starch hydrolysis products with a DE ≤ 6 should be capable of forming a gel network via entanglements, while Castro, Durrieu, Raynaud, and Rouilly (2016) state that entanglements may also be observed for DE ≤ 12.

The master curves of the DE21 and DE38 thin films (Fig. 3F, H) showed dominant viscous behaviour over a wide frequency window of roughly four decades. Above a DE of 20, maltodextrins mostly comprise of short oligomers and small sugars (Loret, Meunier, Frith, & Fryer, 2004) (Table A.3). High DE maltodextrins are known to exhibit viscous behaviour even at relatively high solids concentrations, which is only changed to elastic behaviour upon approaching the glassy state (Siemons et al., 2020; Tsoga et al., 1999). The polysaccharides responsible for the entanglements and hence the rubber plateau for low DE maltodextrins are in high DE maltodextrins replaced by larger fractions of oligomers and small sugars that are more flexible and may reptate sufficiently fast, except in the vicinity of glassy state.

3.2. *Dependence of viscoelastic behaviour on temperature and concentration*

As moisture content and temperature are continuously evolving during drying, we further examined rheological behaviour of maltodextrins over a range of temperatures (10 °C–70 °C) and concentrations (61.8% (w/w) - 95.0% (w/w) solids). From the data we constructed G′ and G″ master curves as described by Marin-Graessley (MG) model (Fig. 4). The logarithm of the horizontal shift factors log (a_T) describes the combined effect of moisture concentration and temperature and is scaled with $(T/T_g\text{-}0.77)^{-1}$ (Fig. 5). Fitted model parameters are provided in Table 2.

For maltodextrin DE5 the master curve covers values from ~$10^{3.9}$ to $10^{8.7}$ Pa and a frequency range of twelve orders of magnitude (Fig. 4A and B). The master curves illustrate the presence of a rubbery plateau

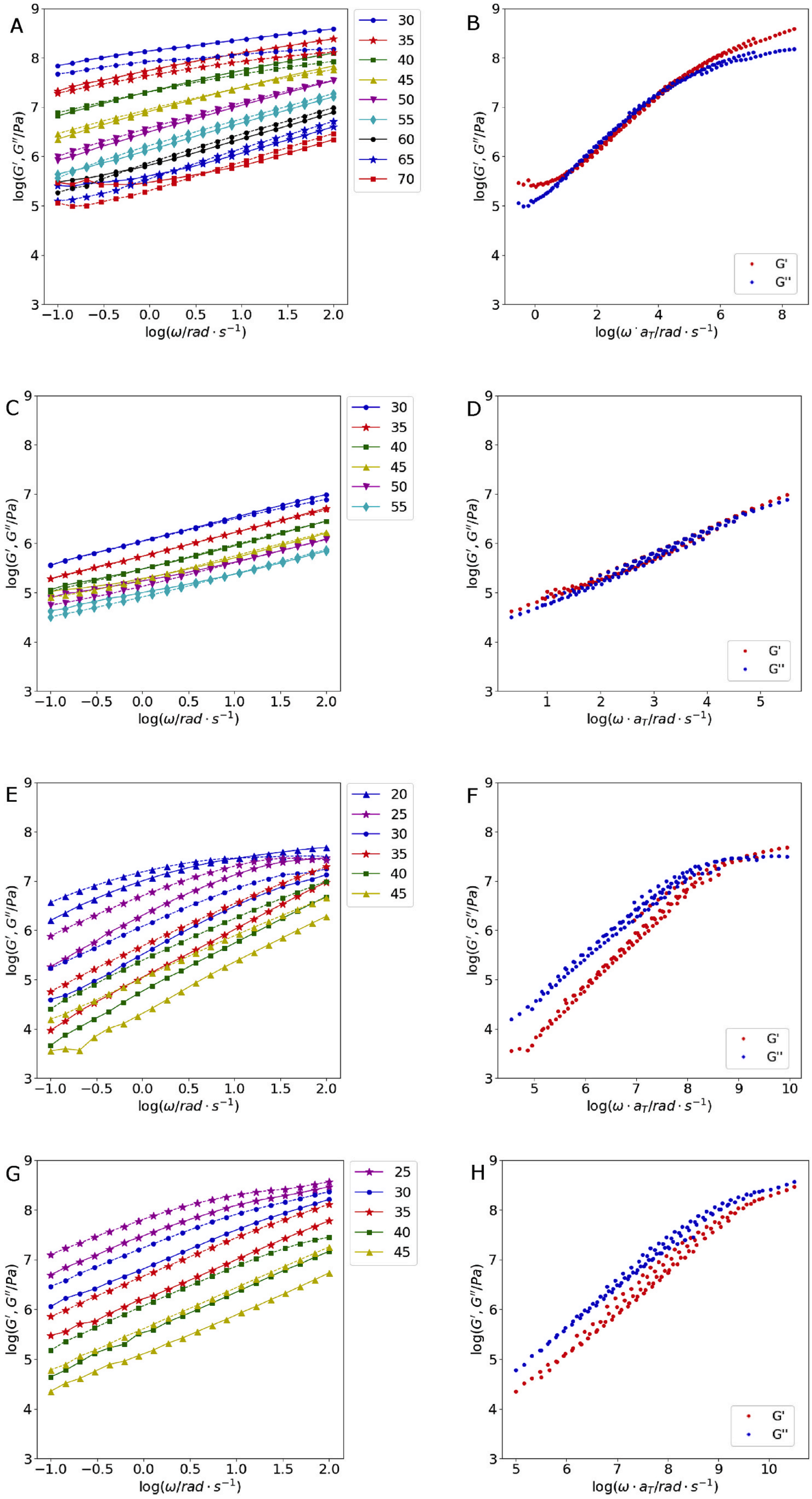

Fig. 3. Left graphs are example mechanical spectra showing the frequency dependence of G' (straight lines) and G'' (dashed lines) of maltodextrin thin films at various temperatures (°C) as indicated in the legends and right graphs show the master curve (G′ red circles and G″ blue circles) of maltodextrin thin films obtained by horizontal superposition along the frequency axis (A, B = DE5 at 84.1% (w/w), C, D = DE12 at 83.8% (w/w), E, F = DE21 at 85.1% (w/w), G, H = DE38 at 95.0% (w/w)). (For interpretation of the references to colour in this figure legend, the reader is referred to the Web version of this article.)

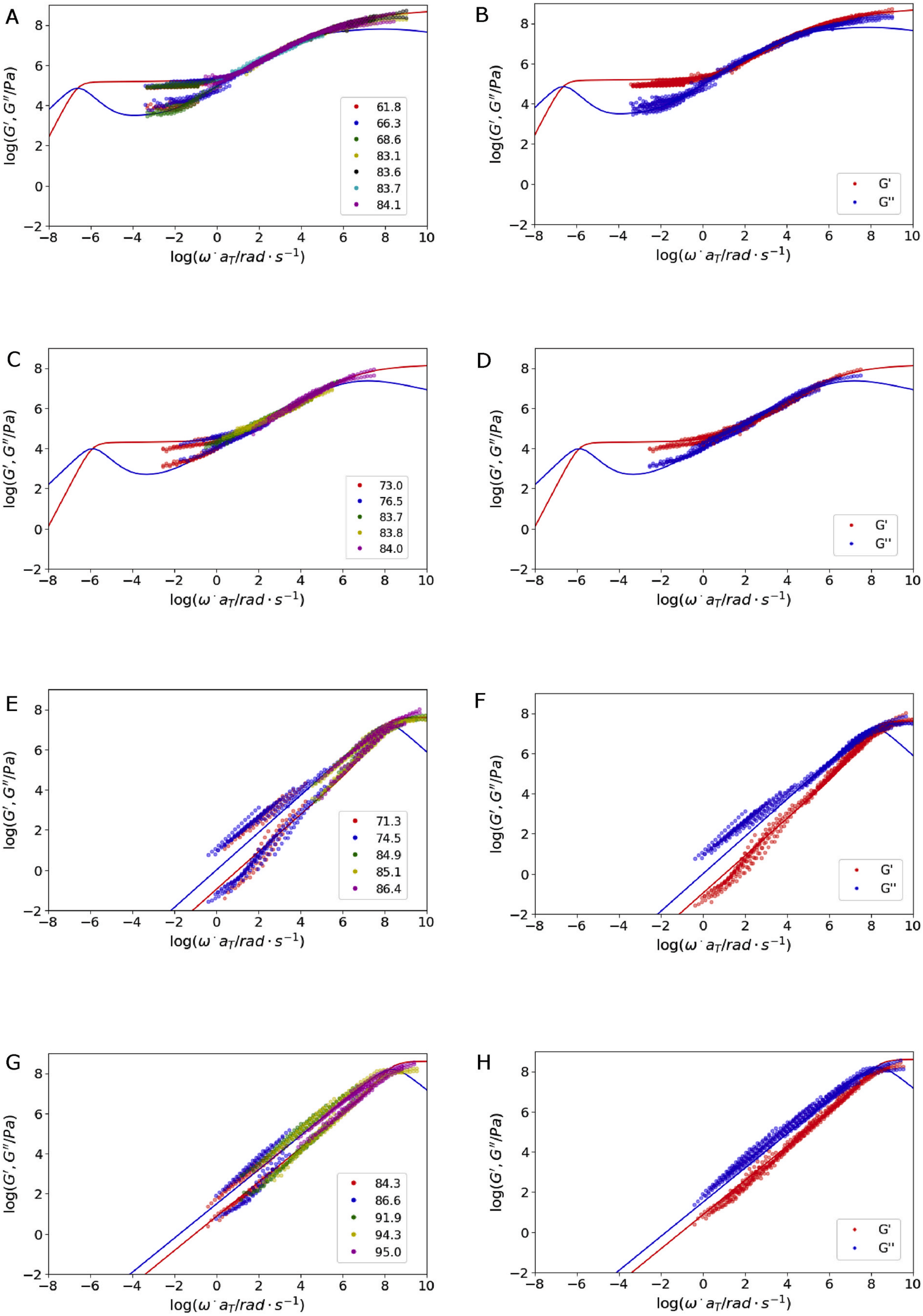

Fig. 4. Master curve G′ and G″ fitted to MG model for DE5 (A, B), DE12 (C, D), DE21 (E, F) and DE38 (G, H). The solids concentrations (% (w/w)) are indicated in different colours in the legends of A, C, E, G. Predicted G′ and G″ are given in lines, red for G′ and blue for G’’. (For interpretation of the references to colour in this figure legend, the reader is referred to the Web version of this article.)

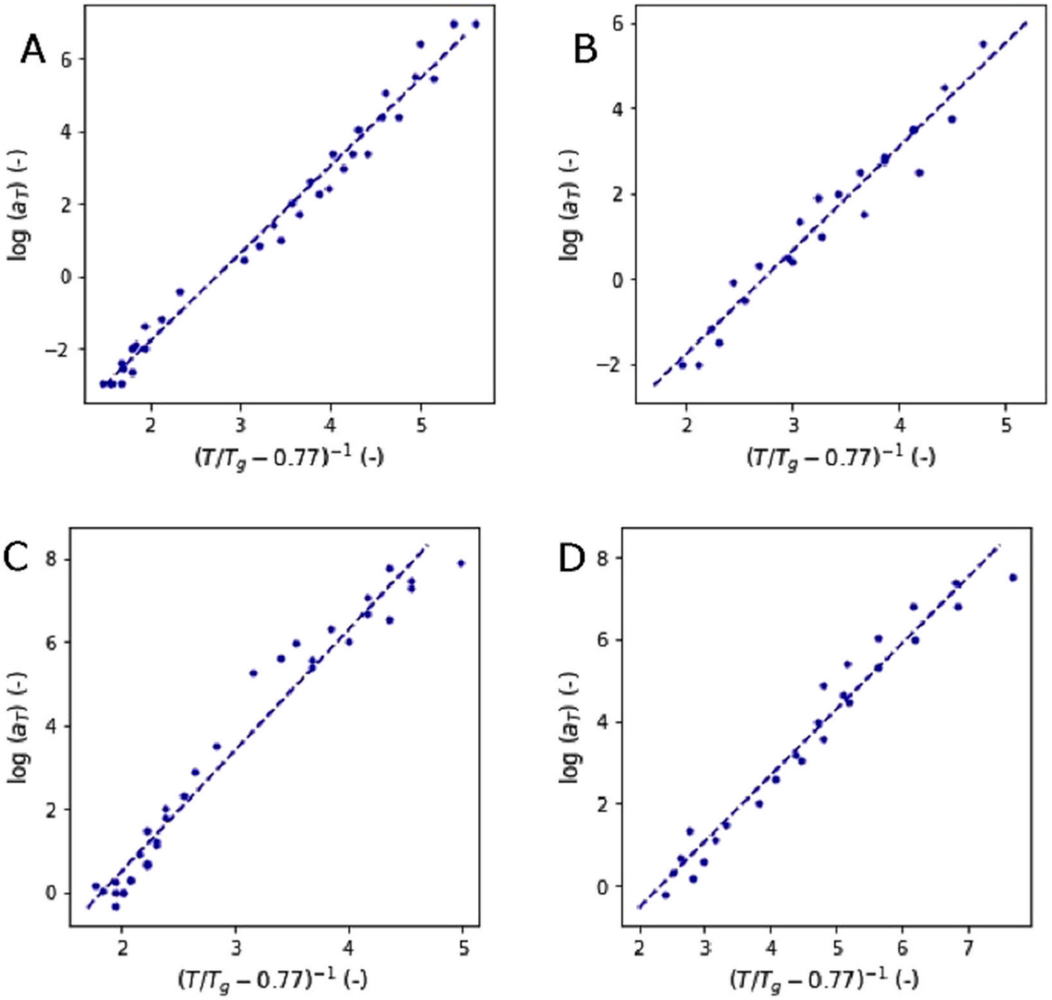

Fig. 5. Horizontal shift factors (a_T) required to construct master curves as function of $(T/T_g\text{-}0.77)^{-1}$ for DE 5 (A), DE12 (B), DE21 (C), DE38 (D). T_g is based on the moisture concentration of the sample as estimated with Couchman-Karasz and T is the experimental temperature of the mechanical spectra. Dotted lines are obtained by fitting with $\log a_T = a\left(\frac{T}{T_g} - 0.77\right)^{-1} + b$.

zone at low frequencies, followed by a remarkable rise in viscoelasticity, which is recognized as the transition region to glassy behaviour (Ferry, Grandine, & Fitzgerald, 1953; Groot & Agterof, 1995). The scaling exponent α was 0.65, resulting in dominating loss modulus in the transition zone. Similar scaling in the transition zone was reported by van der Sman (2021) for maltodextrin DE2 ($\alpha = 0.6$). As the frequency increases beyond the capability of the polysaccharides to respond, i.e. polysaccharides cannot attain their dynamic equilibrium configuration on the timescale of observation, the material glassifies and responds as a hard elastic solid (Ngai, 2011). In the glassy state the storage modulus may reach a maximum value of roughly 10^9 Pa and the loss modulus is expected to decrease (Sperling, 2001). This is however not clearly observed from Fig. 4, however it is more prominent in work reported by for instance Kasapis (2001) and Van der Sman et al. (2021). The MG model describes the experimental data well, even though the experimental loss moduli deviate from the model at higher frequency values. This may be improved by obtaining the modulus in the glassy state, which in this model was based on roughly the highest G' value measured for thin films, even we know that the elastic modulus further increases as solids concentration increases or the temperature decreases beyond the range tested. The model also predicts the rheological behaviour at lower frequencies beyond the frequency range covered by the experimental data, where increased molecular motion as a consequence of increased temperature/decreased concentration may cause assemblies of polysaccharide chains to move in a coordinated manner and accordingly exhibit viscous flow (Sperling, 2001).

A similar viscoelastic pattern was observed for maltodextrin DE12 (Fig. 4C and D), with the scaling exponent α of 0.60 close to 0.65 for DE5 and similar as was found by Van der Sman et al. (2021). Though the plateau modulus (G_N) differed from DE5 as the elastic modulus decreased from about 10^5 to roughly 10^4 Pa. We attribute this to a decreased concentration of long polymeric chains and hence a decreased crosslinking density of the polysaccharides (Ferry, 1980) (Fig. A.2 and Table A.3). Additionally, a higher DE (and thus lower average molecular weight) of the maltodextrins may result in decreasing plateau modulus as a consequence of decrease in molecular weight (Avaltroni et al., 2004; Marin & Graessley, 1977; Rong, Sillick, & Gregson, 2009; Sunthar, 2012).

Master curves constructed for maltodextrins DE21 (Fig. 4E and F) and DE38 (Fig. 4G and H) show an analogous development in the moduli ranging over roughly eight orders of magnitude. For both maltodextrins G″ dominates G' over a broad range of frequencies, while at high frequencies the onset of a cross-over is visible which could signify the vicinity of the glass transition. The scaling exponent α approaches 1 and is 0.93 and 0.85 for DE21 and DE38, respectively. If the scaling exponent α is 1, following Cox-Merz, it suggests the system is behaving as a Newtonian fluid in the transition zone. Additionally, high DE maltodextrins did not exhibit rubber-like behaviour as may be explained by the absence of sufficiently high concentration polysaccharides to form an entangled network (Table A.3). High DE maltodextrins instead have a large fraction of small sugars present which may act as plasticizers, separating the polysaccharides from each other and making disentanglement easier. Due to the absence of a plateau region for high DE maltodextrins, the MG model is simplified by removing the third term of the model (which is required to broaden and flatten the response in the plateau zone) and k_α and τ_α are significantly increased (Marin & Graessley, 1977; Van der Sman et al., 2021). This then results in such low G_N values that the plateau zone is not involved in fitting of the model to the data. Practically, this implies fitting the model in absence of a plateau.

The horizontal shift factors required for the construction of the master curves that capture both the effect of temperature and moisture concentration are shown in Fig. 5. Van der Sman et al. (2021) demonstrated that the horizontal shift factors for highly concentrated maltodextrins and starch are a function of T_g/T. Liu et al. (2006) also investigated the applicability of scaling the shift factors using T_g/T obtained by TTSP by comparing a variety of amorphous polymers and copolymers in the Arrhenius as well as non-Arrhenius regions (T_g/T from 0.5 to 1). They found a universal linear relation between log a_T and $T_g/(T\text{-}0.77T_g)$ with a slope of 3 in Arrhenius and non-Arrhenius regions. We indeed find a linear relation between log a_T and $T_g/(T\text{-}0.77T_g)$ for all the maltodextrins, where slopes vary from 1.6 to 2.9 depending on the DE. A universal slope of 3 was established for a variety of polymers by Liu et al., however as can be seen from the molecular weight distributions maltodextrins are mixtures of polymers, oligomers and sugars which may have caused the slope to diverge from the universal value found for polymers (Fig. A.2).

3.3. Linking rheological data to skin formation and morphology development

To illustrate the added value of the rheological data, we here discuss how rheological behaviour can be connected to morphology development during drying of solutions of maltodextrin DE5 (Fig. 6) and DE38 (Fig. 7). It should be noted that ideally one would view compression of the droplet rather than shearing. However, since the Poisson ratio of maltodextrins can be set at 0.5 as proposed by Dupas-Langlet et al. (2019) and Normand, Plucknett, Pomfret, Ferdinando, and Norton (2001), the master curves constructed from shear rheology will still be useful for explaining the rheological evolution during droplet drying and accordingly the morphology development.

The drying kinetics could be described well with the model until inception of the skin, i.e. locking points (Figs. 6A, 7A, S7, S8). For DE38 the radius decreased a bit faster than the model predicted, which may be due to experimental variations in air and plate temperature. Based on the modelled drying kinetics, the shifted frequencies (shear rates) acting on the different droplet shells were predicted over drying time (Figs. 6B and 7B). The shifted frequencies evolved differently for the different shells of the droplet, accordingly resulting in a distinct evolution of the rheological properties for the different shells (Figs. 6C and 7C).

For the DE5 droplet, G″ is larger than G′ for all inner shells, whereas middle and outer shells showed decreasing G″ for higher frequencies, eventually resulting in elastic behaviour (G’>G″) (Fig. 6C and D). The inner part of the droplet can therefore be characterised as viscoelastic

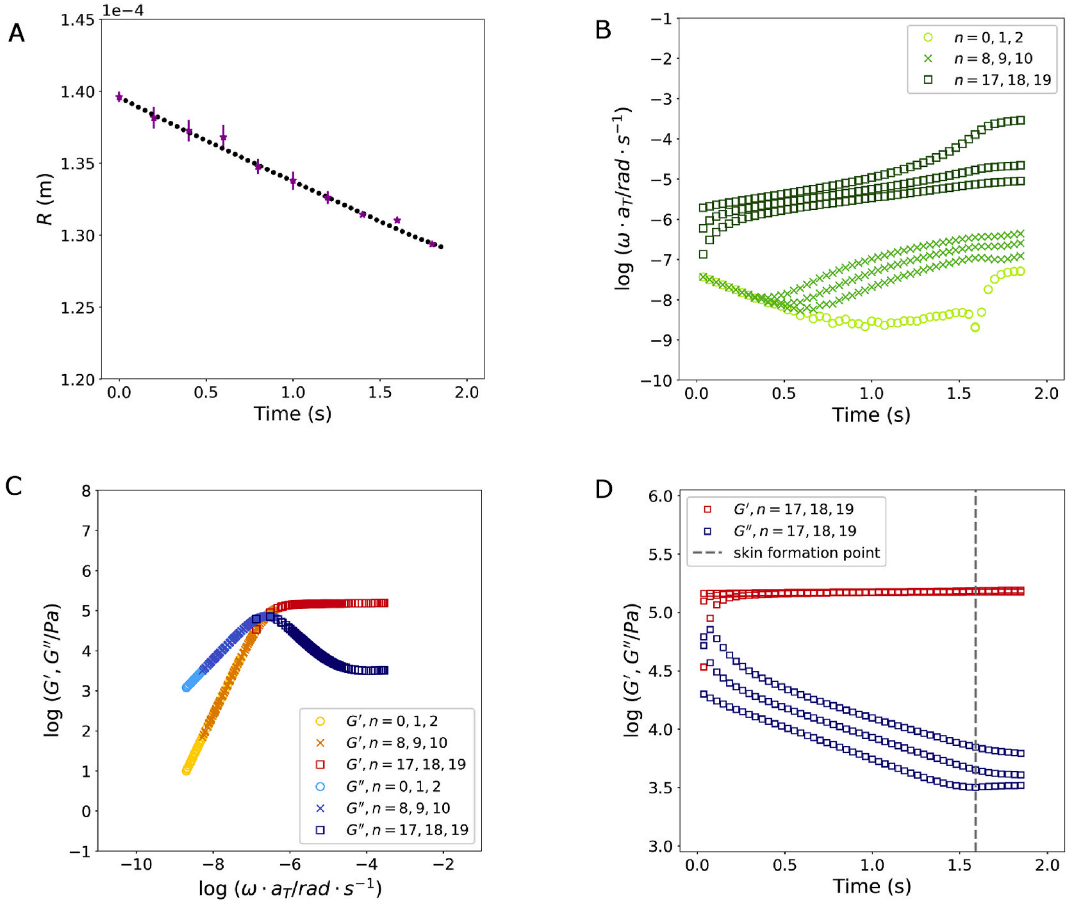

Fig. 6. Radius decrease over time for single droplet drying of DE5 (30% (w/w) initial solids, air temperature 90 °C, air velocity 0.3 m/s) (A), SSE = $1.12{\cdot}10^{-12}$ m^2. Shifted frequency log $\omega{\cdot}a_T$ over drying time for different shells n (with n = 0,1,2 for the inner shells, n = 8,9,10 for middle shells and n = 17,18,19 for outer shells) (B). G′ and G″ as function of shifted frequency log $\omega{\cdot}a_T$ (C). G′ and G″ as function of drying time for outer shells n = 17,18,19 (D).

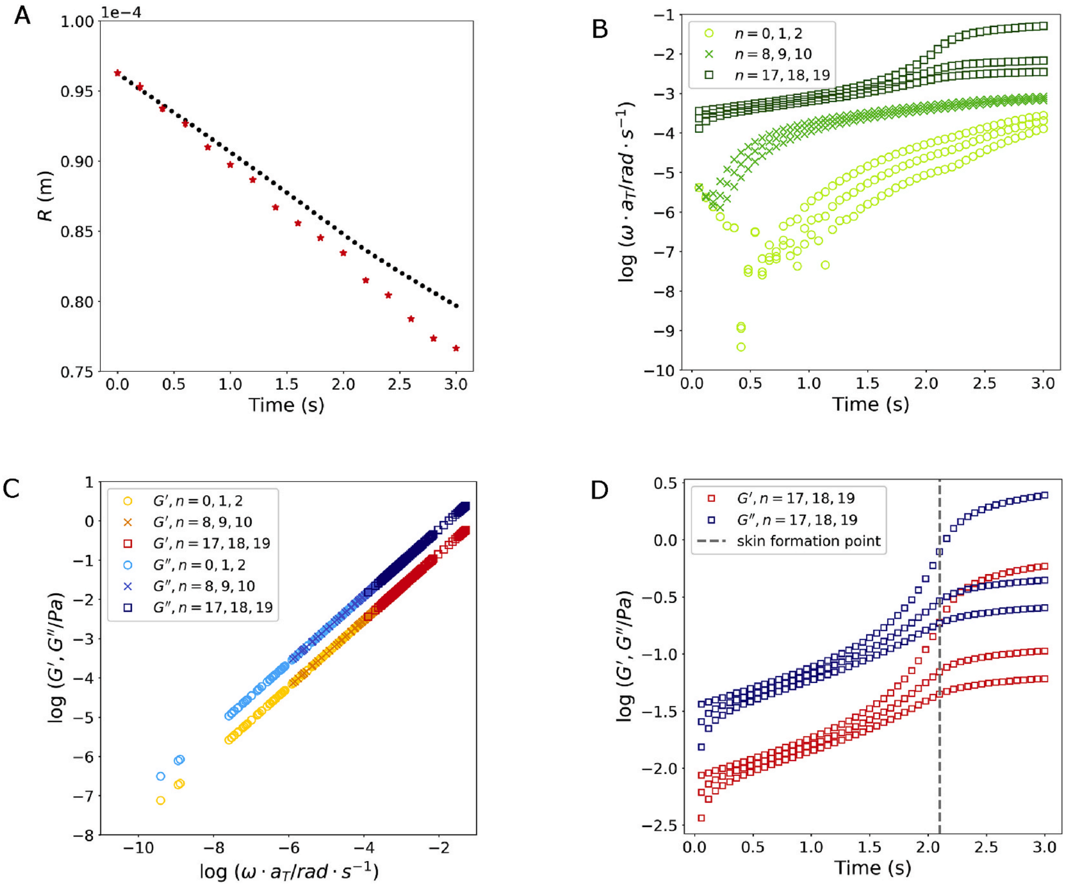

Fig. 7. Radius decrease over time for single droplet drying of DE38 (30% (w/w) initial solids, air temperature 90 °C, air velocity 0.3 m/s) (A), SSE = $4.92 \cdot 10^{-11}$ m^2. Shifted frequency log $\omega \cdot a_T$ over drying time for different shells n (with n = 0,1,2 for the inner shells, n = 8,9,10 for middle shells and n = 17,18,19 for outer shells) (B). G′ and G″ as function of shifted frequency log $\omega \cdot a_T$ (C). G′ and G″ as function of drying time for outer shells n = 17,18,19 (D).

liquid for the drying times investigated, while the middle and outer part showed a transition from a viscous material to an elastic material during drying. It is interesting to note that the elasticity of the skin is not caused by a strong increase of the storage moduli, but by a decrease of the loss moduli. For the DE38 droplet, G″ is always higher than G’ (tan δ = G’’/G’»1) for all droplet shells, which suggests that both the interior and the skin remain viscous throughout the drying process (Fig. 7C and D). Other droplets studied for DE5 and DE38, confirmed the observed trends (Figs. S9 and S10).

Based on the rheological results as a function of the drying time, we attempted to define a skin formation moment. This was done as our hypothesis was that the rheological properties of the outer layers of the droplet at the skin formation moment can help explain the evolution of the surface during drying. The skin can be considered a concentrated region of polymer that has viscoelastic properties distinctively different from that of the core bulk solution (Meng et al., 2014). Therefore, we defined the skin formation moment as the point of steepest increase in log *G*′ of the outer shell in combination with a characteristic change in tan δ was considered (Figs. 6D and 7D). For this, the derivative of log *G*’ was determined by finite difference method and the maximal value of the derivative was selected as skin formation time; tan δ as function of drying time also showed a clear change in slope at this skin formation time (Fig. S11). Using this approach, the skin formation moment for DE5 was roughly 0.5 s earlier than DE38 (1.6 s and 2.1 s, respectively). This earlier skin formation for low DE maltodextrins was previously suggested based on locking point analysis, where the locking points serve as an indirect visual indication for the inception of the skin as aforementioned in section 2.5 (Siemons et al., 2020).

As previously mentioned, we consider the rheological properties of the outer layers at skin formation important in explaining the mechanical instabilities occurring later during drying. For maltodextrin DE5 at the defined skin formation point, dominant elastic behaviour is predicted for the outer shells of the droplet (Fig. 6D). This is likely the consequence of entanglements of the polysaccharides present. Elasticity is suggested important for explaining cavity formation (Bouman et al., 2016; Du et al., 2020). When an elastic/gelled skin is formed at the surface that is still permeable to moisture, ongoing evaporation of moisture from the core of the droplet will result in a skin with increased rigidity. At some point during drying the rigidification of the skin hampers further shrinkage, resulting in a decreasing pressure difference between the inside and outside of the droplet. This results in an inward elastic stress at the weakest point of the skin and consequently cavity formation (Fig. 8A). As soon as a cavity is formed, the pressure difference is eliminated, the compression stress on the skin is removed and wrinkling phenomena are repressed, eventually resulting in a smooth and hollow particle (Du et al., 2020). During skin formation moment for DE38, dominant viscous behaviour of all layers including the outer layers of the droplet is predicted. The droplet may therefore be considered a soft, viscous sphere and with increasing shrinkage, the pressure difference over the outer layers due to water evaporation leads

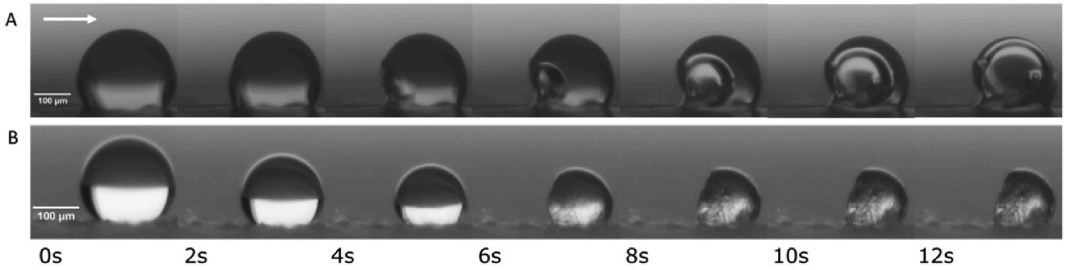

Fig. 8. Particle morphology development (R_0 100 ± 40 µm) during single droplet dying at 90 °C of maltodextrin DE5 30% (w/w), initial contact angle = 125° (A), maltodextrin DE38 30% (w/w), initial contact angle = 142° (B). Air flow (0.3 m/s) came from the left as indicated in the figure by the arrow. Scale bars of 100 µm are provided.

to viscous deformation and wrinkle development (Fig. 8B) (Du et al., 2020; Li, Jia, Cao, Feng, & Gao, 2011). The pressure/compressional energy is dissipated by viscous deformation and thus is not available to restore/retain the spherical shape as it is the case for the elastic skin of DE5 (Brinson & Brinson, 2015; Sperling, 2001).

4. Conclusions

Small amplitude oscillatory shear data of maltodextrins with different DE values as function of temperature and concentration could be mapped onto master curves for G′ and G″ as described with a model for transient/entangled polymeric networks.

Low DE maltodextrins, containing a sufficiently large fraction of polysaccharides, showed a rubber-to-glass transition, whereas high DE maltodextrins mostly consisting of small sugars and oligomers exhibited viscous behaviour over a large range of frequencies. The presence of a rubber plateau zone for low DE maltodextrins is likely the consequence of physical entanglements at sufficiently high concentrations of polysaccharides. The logarithm of the horizontal shift factors for constructing the master curves could be linearly scaled with $T_g/(T\text{-}0.77T_g)$, therefore incorporating both the effect of moisture and temperature. We thus show a Time-Temperature-Concentration superposition principle for these systems.

Finally, we demonstrate that the rheological behaviour can be linked to droplet drying via a numerical model validated with single droplet drying experiments. The rheological properties of the skin formed at the surface of the droplet could indeed be related to the occurrence of surface instabilities i.e. cavitation or wrinkling.

Therefore, the morphology of the droplets for instance generated with spray drying can be predicted using the rheological properties of the materials. This will be a great help in guiding spray drying processes towards desired morphologies and powder properties.

Declaration of interests

The authors declare that they have no known competing financial interests or personal relationships that could have appeared to influence the work reported in this paper.

CRediT authorship contribution statement

I. Siemons: Conceptualization, Methodology, Investigation, Formal analysis, Writing – original draft. **J. Veser:** Methodology, Investigation, Formal analysis, Writing – original draft. **R.M. Boom:** Conceptualization, Writing – review & editing. **M.A.I. Schutyser:** Funding acquisition, Conceptualization, Supervision, Writing – review & editing. **R.G.M. van der Sman:** Funding acquisition, Conceptualization, Supervision, Writing – review & editing.

Acknowledgements

This research is supported by the Netherlands Organization for Scientific Research (NWO) (grant number 15459). We would like to thank Guus Timmermans for supporting this work.

Appendix A. Supplementary data

Supplementary data to this article can be found online at https://doi.org/10.1016/j.foodhyd.2021.107442.

Appendix

Table A.1
Thin films for rheology measurements were prepared by partial drying of the solutions in an oven set at 80 °C, followed by an equilibration step in a climate chamber. Sample volumes, oven times and relative humidity (RH) of the climate chamber are indicated. NA indicates no partial drying in an oven was required prior to the climate chamber. Range of dry matter contents are provided.

DE	Volume (mL)	Oven time (min)	RH (%)	D.M.% (w/w)
5	6–7	115	82–90	81–84
12	6–7	115	80–85	83–84
21	6–7	NA	65–71	84–86
38	5–6	NA	50–55	92–95

Table A.2
Parameter definitions, values and respective model symbols, sources of values are as indicated in the text.

Parameter	Definition	Value
a_{FF}	Flox-Flory fitting parameter ($J \cdot mol^{-1} K^{-1}$)	$5.00 \cdot 10^4$
$C_{p,s}$	Heat capacity of solute ($J \cdot kg^{-1} K^{-1}$)	1000
$C_{p,w}$	Heat capacity of vapour ($J \cdot kg^{-1} K^{-1}$)	1996
$C_{p,w}$	Heat capacity of water ($J \cdot kg^{-1} K^{-1}$)	4200
D_0	Diffusivity constant ($m^2 \cdot s^{-1}$)	$1.39 \cdot 10^{-7}$
D_{air}	Diffusion coefficient of air ($m^2 \cdot s^{-1}$)	$2.42 \cdot 10^{-7}$
$\Delta C_{p,s}$	Change in specific heat of solute ($J \cdot mol^{-1} K^{-1}$)	420
$\Delta C_{p,w}$	Change in specific heat of water ($J \cdot mol^{-1} K^{-1}$)	1910
dE	Activation energy to overcome neighbouring attraction ($kJ \cdot s^{-1}$)	1980
$dH_{evap,0}$	Heat of vaporization of water at 0 °C ($J \cdot kg^{-1}$)	$2.50 \cdot 10^6$
Dt	Iteration time step (s)	0.001
k_B	Boltzmann constant ($J \cdot K^{-1}$)	$1.38 \cdot 10^{23}$
$K_{s,s}$	Free volume parameter for solute (K)	69.21
$K_{s,w}$	Free volume parameter for water (K)	−19.73
$K_{w,s}$	Free volume parameter for solute ($m^3 \cdot kg^{-1} \cdot K^{-1}$)	$3.36 \cdot 10^{-4}$
$K_{w,w}$	Free volume parameter for water ($m^3 \cdot kg^{-1} \cdot K^{-1}$)	$1.95 \cdot 10^{-3}$
N	Total number of shells (−)	20
p_0	Atmospheric pressure (Pa)	$1.00 \cdot 10^5$
Q_D	Thermodynamic factor of Darken relation (−)	1.00
R_{gas}	Ideal gas constant ($J \cdot K^{-1} \cdot mol^{-1}$)	8.31
$T^{\infty}_{g,s}$	Glass transition of solute in infinity (K)	475
$T_{g,w}$	Glass transition temperature of water (K)	136
$V_{c,s}$	Specific critical free volume of solute ($m^3 \cdot kg^{-1}$)	0.59
$V_{c,w}$	Specific critical free volume of water ($m^3 \cdot kg^{-1}$)	0.91
X_p	Distance from droplet place on plate (m)	0.02
η_0	Zero viscosity of solute solution (Pas)	$2.20 \cdot 10^{-4}$
η_W	Viscosity of water (Pas)	$1.00 \cdot 10^{-3}$
λ_s	Thermal conductivity of solute ($W \cdot m^{-1} \cdot K^{-1}$)	0.33
ξ_b	Ratio of solvent and jumping units (−)	0.79
χ_0	Interaction parameter of water (−)	0.50

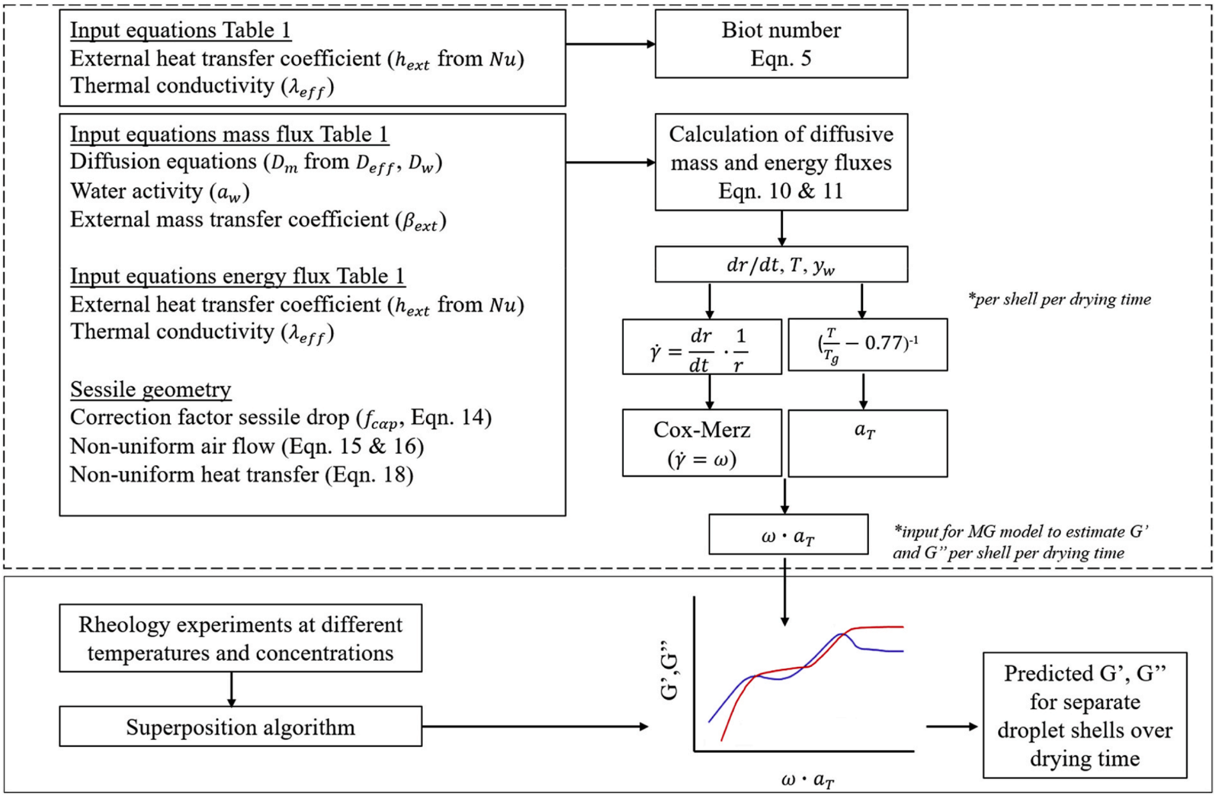

Fig. A.1. Overview of the procedure for calculations as described in sections 2.4-2.6. The top dashed rectangle indicates the single droplet drying model for obtaining the modelled radius decrease, droplet temperature, moisture concentration, and accordingly the shifted frequencies (ω a_T) and the bottom rectangle indicates the coupling of the drying model to the rheological model to predict the rheological properties of the droplet shells over drying time.

Molecular weight distributions

Molecular weight distributions of the different maltodextrins were determined by High Performance Liquid Chromatography (HPLC) using a Shodex KS-802 (7 μm) 8.0 × 300 (mm) + Guard column. The column is operated at 50 °C and connected to a refractive index (RI) detector (Shodex RI-501). Milli-Q water was used as eluent with a flow rate of 1 mL/min. The retention time of maltotridecaose, i.e. maltopolymer with degree of polymerization (DP) of 13, (Elicityl, France) was used to determine the fraction of sugars with a DP above and below 13.

Table A.3
Relative sugar fractions (%) with degree of polymerization (DP) above and below 13 determined by relative peak areas.

DE	>DP13	<DP13
5	77.53	22.47
12	62.77	37.23
21	40.96	59.04
38	18.97	81.03

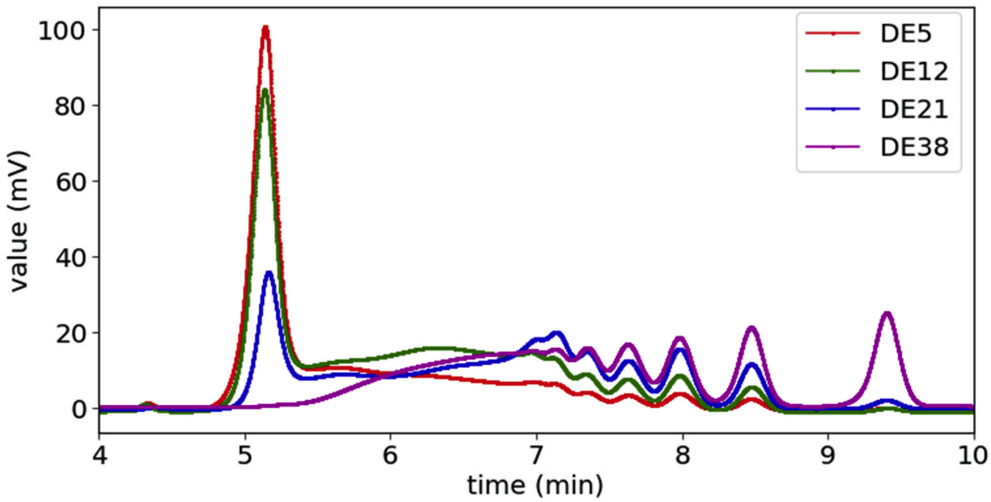

Fig. A.2. Molecular weight distribution for maltodextrin DE5 (red), DE12 (green), DE21 (blue), DE38 (magenta). Molecules with higher molecular weight elute first, followed by low molecular weight components.

References

Adhikari, B., Howes, T., & Bhandari, B. R. (2007). Use of solute fixed coordinate system and method of lines for prediction of drying kinetics and surface stickiness of single droplet during convective drying. *Chemical Engineering and Processing: Process Intensification, 46*(5), 405–419. https://doi.org/10.1016/j.cep.2006.06.018

Augusto, P. E. D., Falguera, V., Cristianini, M., & Ibarz, A. (2013). Viscoelastic properties of tomato juice: Applicability of the Cox-Merz rule. *Food and Bioprocess Technology, 6* (3), 839–843. https://doi.org/10.1007/s11947-011-0655-y

Avaltroni, F., Bouquerand, P. E., & Normand, V. (2004). Maltodextrin molecular weight distribution influence on the glass transition temperature and viscosity in aqueous solutions. *Carbohydrate Polymers, 58*(3), 323–334. https://doi.org/10.1016/j.carbpol.2004.08.001

Both, E. M., Karlina, A. M., Boom, R. M., & Schutyser, M. A. I. (2018). Morphology development during sessile single droplet drying of mixed maltodextrin and whey protein solutions. *Food Hydrocolloids, 75*, 202–210. https://doi.org/10.1016/j.foodhyd.2017.08.022

Both, E. M., Siemons, I., Boom, R. M., & Schutyser, M. A. I. (2019a). The role of viscosity in morphology development during single droplet drying. *Food Hydrocolloids, 94*, 510–518.

Both, E. M., Tersteeg, S. M. B., Boom, R. M., & Schutyser, M. A. I. (2019b). Drying kinetics and viscoelastic properties of concentrated thin films as a model system for spray drying. *Colloids and Surfaces A: Physicochemical and Engineering Aspects*, 585.

Both, E. M., Tersteeg, S. M. B., Schutyser, M. A., & Boom, R. M. (2019c). *Drying kinetics and viscoelastic properties of concentrated thin films as a model system for spray drying*.

Bouman, J., Venema, P., de Vries, R. J., van der Linden, E., & Schutyser, M. A. I. (2016). Vacuole and hole formation during drying of sessile whey protein droplets. *Food Research International, 84*, 16. https://doi.org/10.1016/j.foodres.2016.03.027

Brinson, H. F., & Brinson, L. C. (2015). Polymer engineering science and viscoelasticity: An introduction. In *Polymer engineering science and viscoelasticity: An introduction* (2nd ed.). https://doi.org/10.1007/978-1-4899-7485-3

Castro, N., Durrieu, V., Raynaud, C., & Rouilly, A. (2016). Influence of DE-value on the physicochemical properties of maltodextrin for melt extrusion processes. *Carbohydrate Polymers, 144*, 464–473. https://doi.org/10.1016/j.carbpol.2016.03.004

Couchman, P. R., & Karasz, F. E. (1978). A classical thermodynamic discussion of the effect of composition on glass-transition temperatures. *Macromolecules, 11*(1), 117–119. https://doi.org/10.1021/ma60061a021

Cox, W. P., & Merz, E. H. (1958). Correlation of dynamic and steady flow viscosities. *Journal of Polymer Science, 28*(118), 619–622.

Darken, L. (1948). Diffusion, mobility and their interrelaton through free energy in binary metallic systems. *Transactions of the American Institute of Mining, Metallurgical and Petroleum Engineers, 175*, 184–201.

De Freitas, R. A., Spier, V. C., Sierakowski, M. R., Nicolai, T., Benyahia, L., & Chassenieux, C. (2015). Transient and quasi-permanent networks in xyloglucan solutions. *Carbohydrate Polymers, 129*, 216–223. https://doi.org/10.1016/j.carbpol.2015.04.066

Dealy, J., & Plazek, D. (2009). Time-temperature superposition-a users guide. *Rheology Bulletin, 78*(2), 16–31.

Dupas-Langlet, M., Meunier, V., Pouzot, M., & Ubbink, J. (2019). Influence of blend ratio and water content on the rheology and fragility of maltopolymer/maltose blends. *Carbohydrate Polymers, 213*(November 2018), 147–158. https://doi.org/10.1016/j.carbpol.2019.02.066

Du, G., Ye, F., Doi, M., & Meng, F. (2020). *Drying pathways of an evaporating soft matter droplet*. ArXiv.

Ferry, J. D. (1980). *Viscoelastic properties of polymers*. John Wiley & Sons.

Ferry, J. D., Grandine, L. D., & Fitzgerald, E. R. (1953). The relaxation distribution function of polyisobutylene in the transition from rubber-like to glass-like behavior. *Journal of Applied Physics, 24*(7), 911–916. https://doi.org/10.1063/1.1721401

Finotello, G., Padding, J. T., Deen, N. G., Jongsma, A., Innings, F., & Kuipers, J. A. M. (2017). Effect of viscosity on droplet-droplet collisional interaction. *Physics of Fluids, 29*(6), Article 067102.

Fox, T. G., & Flory, P. J. (1950). Second order transition temperature and related properties of PS. *Journal of Applied Physics, 21*(6), 581–591.

Groot, R. D., & Agterof, W. G. M. (1995). Dynamic viscoelastic modulus of associative polymer networks: Off-lattice simulations, theory and comparison to experiments. *Macromolecules, 28*(18), 6284–6295. https://doi.org/10.1021/ma00122a041

Ishii, M., & Nakamura, H. (2020). Applicability of modified Cox-Merz rule to concentrated suspensions. *Journal of Non-Newtonian Fluid Mechanics*, 282. https://doi.org/10.1016/j.jnnfm.2020.104322. November 2019.

Kasapis, S. (2001). Advanced topics in the application of the WLF/free volume theory to high sugar/biopolymer mixtures: A review. *Food Hydrocolloids, 15*(4–6), 631–641. https://doi.org/10.1016/S0268-005X(01)00048-0

Le Floch-Fouéré, C., Lanotte, L., Jeantet, R., & Pauchard, L. (2019). The solute mechanical properties impact on the drying of dairy and model colloidal systems. *Soft Matter, 15*(30), 6190–6199. https://doi.org/10.1039/c9sm00373h

Levine, H., & Slade, L. (1986). A polymer physico-chemical approach to the study of commercial starch hydrolysis products (SHPs). *Carbohydrate Polymers, 6*(3), 213–244. https://doi.org/10.1016/0144-8617(86)90021-4

Li, B., Jia, F., Cao, Y. P., Feng, X. Q., & Gao, H. (2011). Surface wrinkling patterns on a core-shell soft sphere. *Physical Review Letters, 106*(23), 2–5. https://doi.org/10.1103/PhysRevLett.106.234301

Liu, C., He, J., Keunings, R., & August, R. V. (2006). New linearized relation for the universal viscosity - temperature behavior of polymer Melts. https://doi.org/10.1021/ma061969w, 8867-8869.

Loret, C., Meunier, V., Frith, W. J., & Fryer, P. J. (2004). Rheological characterisation of the gelation behaviour of maltodextrin aqueous solutions. *Carbohydrate Polymers, 57* (2), 153–163. https://doi.org/10.1016/j.carbpol.2004.03.026

Marin, G., & Graessley, W. W. (1977). Viscoelastic properties of high molecular weight polymers in the molten state. *Rheologica Acta, 16*(5), 527–533. https://doi.org/10.1007/bf01525652

Meng, F., Doi, M., & Ouyang, Z. (2014). Cavitation in drying droplets of soft matter solutions. *Physical Review Letters, 113*(9), 1–5. https://doi.org/10.1103/PhysRevLett.113.098301

Mezhericher, M., Levy, A., & Borde, I. (2010). Theoretical models of single droplet drying kinetics: A review. *Drying Technology, 28*(2), 278–293. https://doi.org/10.1080/07373930903530337

Mosaad, M. (1999). Laminar forced convection conjugate heat transfer over a flat plate. *Warme- Und Stoffubertragung Zeitschrift, 35*(5), 371–375. https://doi.org/10.1007/s002310050338

Ngai, K. L. (2011). *Relaxation and diffusion in complex systems*. Springer Science & Business Media.

Normand, V., Plucknett, K. P., Pomfret, S. J., Ferdinando, D., & Norton, I. T. (2001). Large deformation mechanical behavior of gelatin-maltodextrin composite gels. *Journal of Applied Polymer Science, 82*(1), 124–135. https://doi.org/10.1002/app.1831

Palzer, S. (2010). The relation between material properties and supra-molecular structure of water-soluble food solids. *Trends in Food Science & Technology, 21*(1), 12–25. https://doi.org/10.1016/j.tifs.2009.08.005

Patel, K. C., & Chen, X. D. (2008). Surface-center temperature differences within milk droplets during convective drying and drying-based biot number analysis. *AIChE Journal, 54*(12), 3273–3290. https://doi.org/10.1002/aic

Perdana, J., Fox, M. B., Schutyser, M. A. I., & Boom, R. M. (2013). Mimicking spray drying by drying of single droplets deposited on a flat surface. *Food and Bioprocess Technology, 6*(4), 964–977. https://doi.org/10.1007/s11947-011-0767-4

Porfirio, T., Galindo-Rosales, F. J., Campo-Deaño, L., Vicente, J., & Semião, V. (2020). Rheological characterization of polymeric solutions used in spray drying process. *European Journal of Pharmaceutical Sciences, 158*(May 2020), 105650. https://doi.org/10.1016/j.ejps.2020.105650

Rong, Y., Sillick, M., & Gregson, C. M. (2009). Determination of dextrose equivalent value and number average molecular weight of maltodextrin by osmometry. *Journal of Food Science, 74*(1), 33–40. https://doi.org/10.1111/j.1750-3841.2008.00993.x

Roos, Y. H., & Karel, M. (1991). Phase transitions of mixtures of amorphous polysaccharides and sugars. *Biotechnology Progress, 7*(1), 49–53. https://doi.org/10.1021/bp00007a008

Sadek, C., Pauchard, L., Schuck, P., Fallourd, Y., Pradeau, N., Le Floch-Fouéré, C., et al. (2015). Mechanical properties of milk protein skin layers after drying: Understanding the mechanisms of particle formation from whey protein isolate and native phosphocaseinate. *Food Hydrocolloids, 48*, 8–16. https://doi.org/10.1016/j.foodhyd.2015.01.014

Siemons, I., Politiek, R. G. A., Boom, R. M., Sman, R. G. M. Van Der, & Schutyser, M. A. I. (2020). Dextrose equivalence of maltodextrins determines particle morphology development during single sessile droplet drying. *Food Research International, 131* (November 2019), 108988. https://doi.org/10.1016/j.foodres.2020.108988

Siemons, I., Vaessen, E. M. J., Oosterbaan van Peski, S. E., Boom, R. M., & Schutyser, M. A. I. (2021). Protective effect of carrier matrices on survival of Lactobacillus plantarum WCFS1 during single droplet drying explained by particle morphology development. *Journal of Food Engineering, 292*(August 2020), 110263. https://doi.org/10.1016/j.jfoodeng.2020.110263

Sillick, M., & Gregson, C. M. (2009). Viscous fragility of concentrated maltopolymer/sucrose mixtures. *Carbohydrate Polymers, 78*(4), 879–887. https://doi.org/10.1016/j.carbpol.2009.07.015

van der Sman, R. G. M. (2003). Simple model for estimating heat and mass transfer in regular-shaped foods. *Journal of Food Engineering, 60*(4), 383–390. https://doi.org/10.1016/S0260-8774(03)00061-X

Sman, R. G. M. Van Der, & Meinders, M. B. J. (2012). Supplementary Material to : Moisture diffusivity in food materials. *1–11*. June.

Soh, G. Y., Yeoh, G. H., & Timchenko, V. (2016). An algorithm to calculate interfacial area for multiphase mass transfer through the volume-of-fluid method. *International Journal of Heat and Mass Transfer, 100*, 573–581. https://doi.org/10.1016/j.ijheatmasstransfer.2016.05.006

Sperling, L. H. (2001). *Introduction to physical polymer science* (3rd ed.). John Wiley & Sons, Ltd.

Sugiyama, Y., Larsen, R. J., Kim, J. W., & Weitz, D. A. (2006). Buckling and crumpling of drying droplets of colloid-polymer suspensions. *Langmuir, 22*(14), 6024–6030. https://doi.org/10.1021/la053419h

Sunthar, P. (2012). Polymer rheology. *Robust Process Development and Scientific Molding*, 27–41. https://doi.org/10.3139/9783446433427.003

Sutherland, W. (1905). A dynamical theory of diffusion for non-electrolytes and the molecular mass of albumin. *The London, Edinburgh, and Dublin Philosophical Magazine and Journal of Science, 9*(54), 781–785.

Tsoga, A., Kasapis, S., & Richardson, R. K. (1999). The rubber-to-glass transition in high sugar agarose systems. *Biopolymers, 49*(4), 267–275. https://doi.org/10.1002/(SICI)1097-0282(19990405)49:4<267::AID-BIP1>3.0.CO;2-1

Ubbink, J., & Dupas-Langlet, M. (2020). Rheology of carbohydrate blends close to the glass transition: Temperature and water content dependence of the viscosity in relation to fragility and strength. *Food Research International, 138*(PB), 109801. https://doi.org/10.1016/j.foodres.2020.109801

Van Der Sman, R. G. M., & Meinders, M. B. J. (2011). Prediction of the state diagram of starch water mixtures using the Flory-Huggins free volume theory. *Soft Matter, 7*(2), 429–442. https://doi.org/10.1039/c0sm00280a

Van Der Sman, R. G. M., & Meinders, M. B. J. (2013). Moisture diffusivity in food materials. *Food Chemistry, 138*(2–3), 1265–1274. https://doi.org/10.1016/j.foodchem.2012.10.062

Van der Sman, R. G. M., Dupas-Langlet, M., Ubbink, J., Kristiawan, M., & Siemons, I. (2021). Scaling relations in rheology of concentrated starches and maltodextrins. *Food Hydrocolloids* (in press).

van der Sman, R. G. M., & Mauer, L. J. (2019). Starch gelatinization temperature in sugar and polyol solutions explained by hydrogen bond density. *Food Hydrocolloids, 94*, 371–380. https://doi.org/10.1016/j.foodhyd.2019.03.034.

Vrentas, J., & Vrentas, C. (1991). Sorption in glassy polymers. *Macromolecules, 24*(9), 2404–2412.

Wang, H., & Cai, S. (2015). Cavitation in a swollen elastomer constrained by a non-swellable shell. *Journal of Applied Physics, 117*(15), 1–5. https://doi.org/10.1063/1.4918278

Winter, H. H. (2009). Three views of viscoelasticity for Cox-Merz materials. *Rheologica Acta, 48*(3), 241–243. https://doi.org/10.1007/s00397-008-0329-5